Journal of Energy Chemistry 118 (2026) 591–601

Contents lists available at ScienceDirect

Journal of Energy Chemistry

journal homepage: www.elsevier.com/locate/jechem

http://www.journals.elsevier.com/journal-of-energy-chemistry/

# Difluorocarbene grafted on carbon for high-power supercapacitors

Kai Gu [a,1], Zhenyu Chen [a,1], Yuxun Yuan [a], Ting Yang [a], Yihan Wang [a,b,c], Lei Zhou [a], Lingchao Wu [a], Guilin Feng [a,b,*], Weiqing Yang [a,b,*]

[a] Key Laboratory of Advanced Technologies of Materials (Ministry of Education), School of Materials Science and Engineering, Southwest Jiaotong University, Chengdu 610031, Sichuan, China
[b] Research Institute of Frontier Science, Southwest Jiaotong University, Chengdu 610031, Sichuan, China
[c] Institute of Atomic and Molecular Physics, Sichuan University, Chengdu 610065, Sichuan, China

ARTICLE INFO

*Article history:*
Received 8 January 2026
Revised 29 March 2026
Accepted 30 March 2026
Available online 9 April 2026

*Keywords:*
Biomass-derived carbon
Difluorocarbene grafting
Gas-solid reaction
High-power supercapacitors
Electron density redistribution

ABSTRACT

Biomass-derived activated carbon is a highly promising electrode material for supercapacitors. However, its widespread application is often limited by insufficient power density, stemming from low electrical conductivity and sluggish ionic transport. To address these challenges, we developed a difluorocarbene-grafted strategy that fluorinates surface carbonyl groups on carbon through a gas-solid reaction path. This process effectively induces a redistribution of carbon atomic electron density and concurrently reconfigures the microporous-mesoporous architecture. The resultant synergistic effects significantly enhance both charge transport efficiency and ionic storage capacity. The optimized fluorinated macadamia nut shell-derived activated carbon (F-MNSAC) exhibits a remarkable compaction density of 0.64 g $cm^{-3}$, an electrical conductivity of 3.34 S $mm^{-1}$, and a substantial pore volume of 1.213 $m^3$ $g^{-1}$. The supercapacitor based on F-MNSAC delivers a higher specific capacitance (33.63 F $g^{-1}$ at 1 A $g^{-1}$) than commercialized YP-50F (~27 F $g^{-1}$ at 1 A $g^{-1}$), and outstanding rate capability (86.6% capacity retention at 50 A $g^{-1}$). Consequently, the device achieves a high energy density of 24.1 Wh $kg^{-1}$ at a high power density of 61.2 kW $kg^{-1}$. This work establishes a new paradigm for developing high-performance carbon materials and lays a firm technological foundation for advancing next-generation, high-power supercapacitors.

© 2026 Science Press and Dalian Institute of Chemical Physics, Chinese Academy of Sciences. Published by Elsevier B.V. and Science Press. All rights are reserved, including those for text and data mining, AI training, and similar technologies.

## 1. Introduction

The energy storage mechanism of supercapacitors is based on the highly reversible adsorption and desorption of electrolyte ions at the electrode interface. Consequently, their electrochemical performance is intrinsically governed by the microstructure, electronic state, and phase composition of the electrode materials [1–4]. Activated carbon (AC) is widely regarded as the preferred electrode material for high-performance supercapacitors due to its high specific surface area, excellent thermal stability, and chemical inertness [5–7]. Derived from sustainable biomass, macadamia nut shells, as an abundant and low-cost byproduct of the food industry, represent a high-quality precursor for AC synthesis, offering significant potential for value-added application in energy storage [8]. However, biomass-derived ACs often suffer from non-ideal pore size distributions and complex surface chemistries. The former leads to tortuous diffusion pathways and increased ion transport resistance, while the latter introduces abundant defects and polar functional groups that disrupt the conjugated carbon network and act as electron scattering sites. These inherent limitations typically result in sluggish electron transport and ion diffusion kinetics, which hinder rapid electrochemical responses and ultimately constrain the achievable power density of the devices [9–12]. Therefore, developing effective strategies to enhance the intrinsic electronic conductivity and ion mobility of ACs is crucial for boosting power density and ensuring the efficient long-term operation of supercapacitors. Current approaches to simultaneously address these challenges primarily focus on three key strategies: (i) hierarchical pore structure design, (ii) graphitization treatment, and (iii) carbon defect engineering. Hierarchical pore structuring, often achieved via templating methods,

* Corresponding authors.
*E-mail addresses:* guilinf@swjtu.edu.cn (G. Feng), wqyang@swjtu.edu.cn (W. Yang).
[1] These authors contributed equally to this work.

https://doi.org/10.1016/j.jechem.2026.03.057
2095-4956/© 2026 Science Press and Dalian Institute of Chemical Physics, Chinese Academy of Sciences. Published by Elsevier B.V. and Science Press. All rights are reserved, including those for text and data mining, AI training, and similar technologies.

constructs a three-dimensional network of interconnected micro-, meso-, and macropores. This architecture can reduce interfacial resistance and improve electrolyte wettability, thereby enhancing both charge and mass transport [13–15]. However, the involved multi-step processes often impede scalability and industrial adoption [16]. Graphitization treatment, typically employing high-temperature or chemical processes, promotes the rearrangement of carbon atoms into ordered $sp^2$ domains. This improves electrical conductivity and creates smoother pore walls to facilitate ion movement, yet it remains an energy-intensive approach with precise control challenges [17–19]. In comparison, carbon defect engineering via heteroatom doping, such as nitrogen (N) [20–22], oxygen (O) [23,24], phosphorus (P) [25], sulfur (S) [26,27], and fluorine (F) [28–31], offers a versatile route to modify the electron density distribution within the carbon matrix. Among these dopants, F possesses the highest electronegativity. The introduction of F atoms forms highly polarized C–F bonds, which can simultaneously modulate the overall charge distribution of the ACs framework and induce tailored structural defects. This dual effect significantly enhances electrical conductivity and ionic affinity while largely preserving the desirable porous morphology of ACs [29,32]. Thus, F-doping emerges as a promising dual-functional strategy, concurrently enabling precise surface chemical modification and bulk structural optimization. Currently, the fluorination strategies for carbon materials mainly include plasma treatment, solution-based fluorination, and direct gas-phase fluorination. Although these methods are effective in introducing F atoms, they often have issues such as limited selectivity, harsh reaction conditions, or significant damage to the carbon framework [33–36].

Herein, we propose an innovative difluorocarbene ($:CF_2$) grafting strategy that reconfigures the surface chemistry of ACs through a targeted gas-solid reaction. Unlike conventional fluorination methods that introduce F atoms non-selectively, this approach specifically cleaves surface carbonyl (C=O) groups via controlled pyrolysis of polytetrafluoroethylene (PTFE), forming polarized C–F bonds while eliminating oxygen as CO. This selective substitution serves a dual purpose: (i) modulating the electron density distribution within the carbon framework to enhance intrinsic conductivity and (ii) simultaneously transforming the pore architecture by converting a portion of micropores into mesopores, thereby facilitating ion transport. The resulting fluorinated macadamia nut shell-derived activated carbon (F-MNSAC) exhibits significantly enhanced electrical conductivity and a pronounced expansion in mesopore volume. In the supercapacitor device, F-MNSAC delivers a high specific capacitance of 33.63 F $g^{-1}$ at 1 A $g^{-1}$ and demonstrates outstanding rate capability, retaining 86.6% of this capacitance at a high current density of 50 A $g^{-1}$. Consequently, the device achieves an exceptional combination of a high energy density of 24.1 Wh $kg^{-1}$ and a high power density of 61.2 kW $kg^{-1}$. This study provides fundamental design insights and a theoretical framework for engineering next-generation AC materials. These findings pave the way for developing supercapacitors that achieve a well-balanced combination of high power and high energy density, addressing a critical challenge in advanced energy storage systems.

## 2. Results and discussion

### 2.1. Synthesis and characterization of F-MNSAC

Fig. 1 illustrates the design concept of this work. F atoms are introduced into the carbon network via a difluorocarbene grafting mechanism, facilitated by a gas-solid reaction generated from the thermal decomposition of PTFE (Fig. S1). Specifically, PTFE powder placed near the carrier gas inlet underwent near-complete pyrolysis at 650 °C under an argon (Ar) atmosphere (Fig. S2), producing small-molecule fluorocarbon compounds such as tetrafluoroethylene (TFE, $C_2F_4$), hexafluoropropylene (HFP, $C_3F_6$), and octafluorocyclobutane (OFCB, $C_4F_8$). At elevated temperatures, these compounds further dissociated via homolytic cleavage to form highly reactive $:CF_2$ [37]. The $:CF_2$ possesses a compact molecular size (C–F bond length of ~1.30 Å, F–C–F bond angle of ~104.86°) with a kinetic diameter of approximately 2.5 Å, which is significantly smaller than that of a molecule of Ar (~3.4 Å). Due to the small size, $:CF_2$ can freely migrate in the Ar gas flow and reach the surface of the carbon material. Importantly, the kinetic diameter of $:CF_2$ is also smaller than that of a nitrogen ($N_2$) molecule (3.64 Å), the standard probe for evaluating microporosity [38,39]. This size advantage allows $:CF_2$ to penetrate micropores (<2 nm) and even ultra-micropores that are inaccessible to $N_2$, enabling thorough fluorination throughout the bulk material. Transported by the carrier gas, $:CF_2$ was adsorbed onto the AC surface (positioned near the gas outlet) and initiated the grafting process. The proposed grafting mechanism can proceed through three key stages: (i) Formation of a transition state: driven by strong electrophilic-nucleophilic interaction, the carbon atom of $:CF_2$ engages with the lone pair of electrons on the C=O oxygen, forming a C–O bond, while simultaneously interacting with the C=O carbon to initiate a C–C bond. Together, these interactions create an unstable four-membered cyclic transition state; (ii) Decomposition of the transition state: due to significant ring strain, this transition state is highly unstable and rapidly decomposes via the elimination of a carbon monoxide (CO) molecule; (iii) Rearrangement: concurrent with CO evolution, the structure undergoes swift rearrangement, leading to the incorporation of a $>C–CF_2$ moiety into the carbon skeleton. It should be noted that in the resulting $>C–CF_2$ structure, the carbene carbon atom connecting the two F atoms is likely bonded to the carbon framework via one covalent bond, and its fourth valence is accommodated by the conjugated system or adjacent atoms, allowing it to be incorporated into the overall carbon network.

To further uncover the grafting mechanism, the thermogravimetric mass spectrometry (TG-MS) test was carried out on the mixture of MNSAC and PTFE to confirm the production of CO. As shown in Fig. 2(a), the temperature range was set from room temperature to 650 °C, with a hold at 450 °C for 30 min. The MS curves demonstrated the presence of $C_2F_4$, $C_3F_6$, $C_4F_8$, and CO (Fig. S3). That is, $:CF_2$ consumed one C=O while introducing two F atoms throughout this process. Considering that some oxygen-containing functional groups (OCFGs) may also decompose within this temperature range, further quantitative analysis is required. This issue will be explored in subsequent X-ray photoelectron spectroscopy (XPS) analysis. The material obtained via difluorocarbene grafting is denoted as F-MNSAC, while the untreated material is denoted as MNSAC. To verify the successful surface modification of F-MNSAC, a series of characterizations was conducted. Energy dispersive spectroscopy (EDS) analysis was employed to examine the surface elemental distribution. As shown in Fig. 2(b), both materials exhibited C element as the predominant phase, with O element uniformly distributed across the surface. In contrast to MNSAC, distinct and densely distributed F element signals were observed on the surface of F-MNSAC, providing preliminary evidence for incorporation of F. Subsequently, Fourier transform infrared spectroscopy (FT-IR) was employed to investigate the vibrational modes of internal chemical bonds (Fig. 2c). Both the materials displayed broad absorption peaks at 3450 $cm^{-1}$ corresponding to O–H stretching vibrations, attributed to water molecules adsorbed from ambient air. Peaks at 2920 and 2850 $cm^{-1}$ correspond to C–H stretching vibrations within the carbon framework. Peaks at 1630 and 1380 $cm^{-1}$ represent C=C and C–C stretching vibrations within the carbon framework, respectively. Notably,

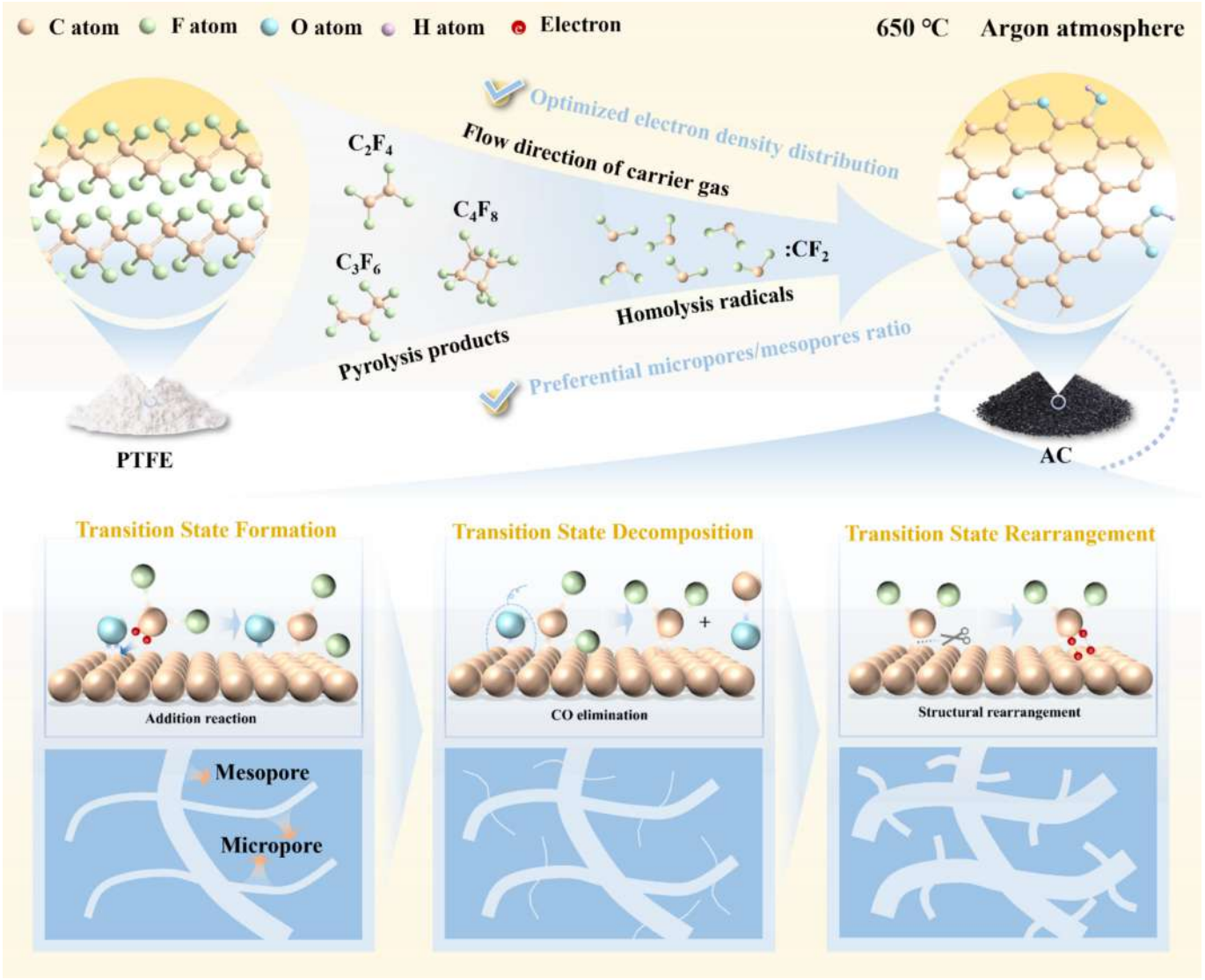



**Fig. 1.** Schematic diagram of the difluorocarbene-grafted strategy.

a distinct and broad C–F absorption peak appeared at 1150 $cm^{-1}$ in F-MNSAC, which confirmed successful F atom bonding to the carbon skeleton [40–42]. Based on the extremely high electronegativity of the F atom and its bonding characteristics with carbon, it can be expected that the resulting C–F bond will be highly polar and primarily covalent in nature. The specific types and distribution of the bond will be explained in subsequent XPS analysis. Interestingly, the O–H peak intensity in F-MNSAC is significantly lower, consistent with the hydrophobic nature of C–F bonds, resulting in reduced adsorption capacity for water molecules. Furthermore, to gain deeper insight into the surface chemical states and bonding configurations, XPS was performed for localized characterization. The XPS survey spectrum in Fig. 2(d) confirms the presence of C, O, and F elements in F-MNSAC, whereas MNSAC contains only C and O elements. High-resolution C 1*s* spectrum, as depicted in Fig. 2(e) and Fig. S4, assigned the deconvoluted peaks at 284.78, 286.28, 287.65, 289.30, and 290.94 eV to C=C/C–C, C–O, C=O, C–F, and O–C=O bonds, respectively [43]. It is worth noting that the obvious C–F component only appears in F-MNSAC, with a relative content of 4.30% (Table S1), confirming that the F atom has been successfully incorporated into the carbon framework. Further fitting analysis of the O 1*s* spectrum (Fig. 2f) was conducted to investigate the evolution of OCFGs during the difluorocarbene grafting process. The peaks at binding energies of 531.13, 532.56, 533.88, and 535.52 eV are assigned to quinone-type oxygen, C=O, ether bonds (C–O–C), and carboxyl groups (–COOH), respectively. Comparative analysis of the content changes in OCFGs shows that the C=O content in F-MNSAC decreased by 2.12% after fluorination (Fig. 2g, Table S2). Surprisingly, the increase in C–F content and the decrease in C=O content basically satisfy a ratio of 2:1, corresponding to the mechanism described earlier. This quantitative relationship, together with TG-MS evidence, indicates that :$CF_2$ preferentially targeted C=O sites during the reaction, introducing F atoms via the replacement of C=O groups. To elucidate the chemical state of the incorporated F element, a high-resolution F 1*s* spectrum was fitted. As depicted in Fig. 2(h), the deconvoluted peaks appeared at 683.34, 686.30, and 689.56 eV, corresponding respectively to covalent C–F bonds, semi-ionic C–F bonds, and ionic C–F bonds, reflecting distinct bonding states formed between F and C atoms due to their differing electronegativities. Among these, the covalent C–F bond predominated, and its strong polarity induced a significant electron-withdrawing effect, contributing to enhanced intrinsic conductivity of F-MNSAC. This aspect will be discussed in detail in the subsequent theoretical calculations section.

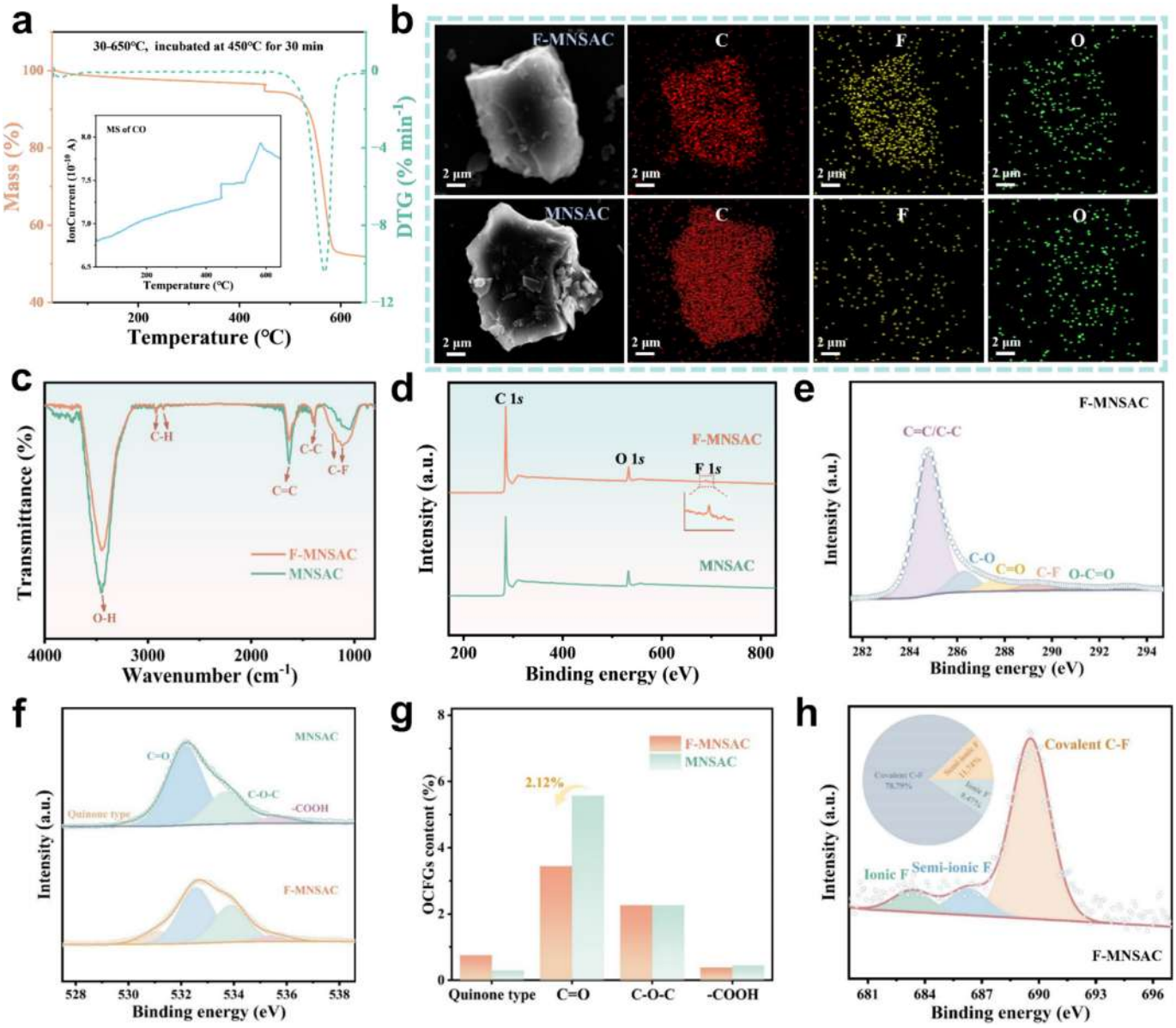



**Fig. 2.** (a) TG-MS of MNSAC and PTFE mixture; (b) SEM images and EDS mapping; (c) FT-IR spectra; (d) XPS survey spectra; (e) high-resolution C 1*s* XPS spectrum; (f) high-resolution O 1*s* XPS spectrum; (g) comparative quantitative analysis of OCFGs; (h) high-resolution F 1*s* XPS spectrum of F-MNSAC and MNSAC.

Prior studies have indicated that heteroatom doping often disrupts the π-π conjugation within the carbon network, reducing intrinsic conductivity and impeding ion transport [44]. Nevertheless, four-probe measurements revealed that F-MNSAC exhibited a high compaction density of 0.64 g $cm^{-3}$ (Fig. 3a) and a superior conductivity of 3.34 S $mm^{-1}$ (Fig. 3b) at equivalent yield strength. This phenomenon stems from F atom-induced potential redistribution, which establishes efficient electron leakage pathways, thereby preserving the excellent electronic transport capability of the material. The microcrystalline structure was characterized via X-ray diffraction (XRD). As presented in Fig. 3(c), both F-MNSAC and MNSAC displayed characteristic broad diffraction peaks at approximately 26° and 44°, corresponding to the (002) and (100) planes of graphite, respectively. The broadened features suggest a predominantly amorphous structure, which is closely related to defects. Defect levels were assessed using Raman spectroscopy. As shown in Fig. 3(d), both materials exhibited two broadened double-peak structures, namely the disordered (D) band (1357 $cm^{-1}$) and graphite (G) band (1589 $cm^{-1}$), characteristic of amorphous carbon. The D band originated from vibrations at $sp^3$-hybridised carbon edges and defects, whilst the G band corresponded to stretching vibrations of $sp^2$-hybridised carbon within rings or chains. Deconvolution of the Raman spectra revealed additional peaks (Table S3). The D2 peak (~1620 $cm^{-1}$) is attributed to the $E_2g$ vibration mode induced by surface graphite layer disorder or defects. The D3 peak (~1500 $cm^{-1}$) usually corresponds to amorphous carbon. The D4 peak (~1190 $cm^{-1}$) belongs to vibrations related to disordered graphite lattices, polyene structures, or the $sp^2$-$sp^3$ interface [45]. Multi-peak structure indicates a composite architecture where defects coexist with ordered domains. The intensity ratio of the D band to G band ($I_D/I_G$) is commonly used to evaluate the disorder degree in carbon materials [46]. F-MNSAC exhibited a higher $I_D/I_G$ ratio of 3.19, compared to 2.99 for MNSAC, indicating that the difluorocarbene grafting process introduces additional structural defects and reduces the degree of ordered stacking of graphitic microcrystals. In addition, the D3

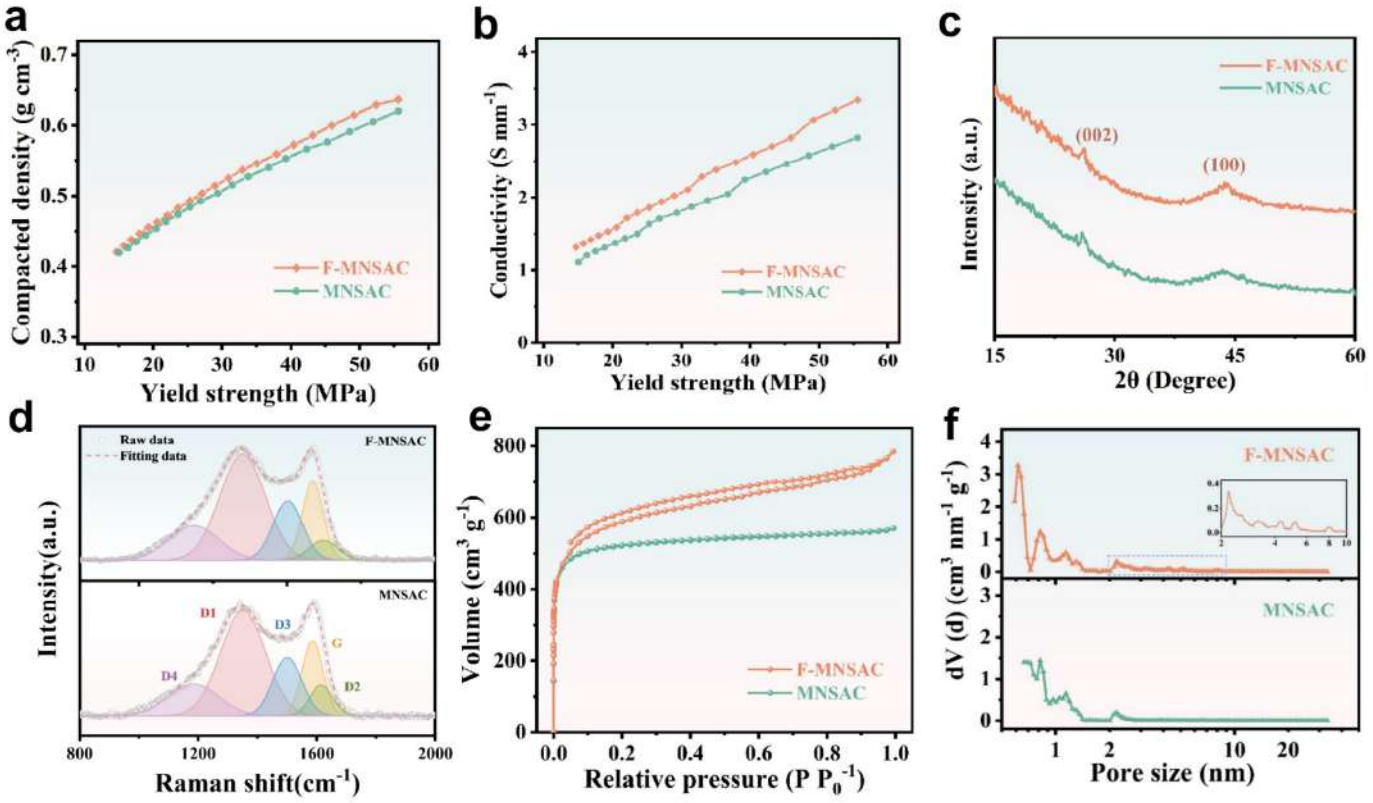



**Fig. 3.** Lattice structure and physicochemical properties of F-MNSAC and MNSAC. (a) Powder compaction density as a function of yield strength; (b) electrical conductivity as a function of yield strength; (c) XRD patterns; (d) Raman spectra; (e) $N_2$ adsorption/desorption isotherms; (f) the corresponding pore size distribution curves.

peak area of F-MNSAC increased, indicating an enhancement of $sp^2$-$sp^3$ hybrid structures. This observation is consistent with the proposed grafting mechanism, in which each consumed C=O group introduces two C–F bonds that contribute to the D3 peak. Defect structure significantly influences the morphology and pore distribution of ACs. Scanning electron microscope (SEM) images revealed that F-MNSAC exhibited an irregular, fragmented morphology (Fig. S5), resulting from particle structure dissociation during the vigorous chemical activation process, which aligns with its particle size distribution map (Fig. S6). After comparison with MNSAC, it can be found that the fluorination process has no significant effect on the morphology of F-MNSAC. High-resolution SEM revealed a relatively smooth surface on F-MNSAC without obvious large pores, suggesting a dense structure. This compactness will help mitigate stress concentration during long-term charge/discharge cycling, suppress pore structure collapse, and thereby enhance electrode structural stability and device longevity. Transmission electron microscopy (TEM) further revealed the pore structure at the nanoscale (Fig. S7). F-MNSAC and MNSAC both possessed abundant micropores, which served as storage sites for electrolyte ions. Concurrently, graphite microcrystals were randomly embedded within an amorphous carbon skeleton, building a locally ordered but overall disordered structure conducive to rapid electron transport and efficient charge storage. $N_2$ adsorption-desorption testing further elucidated the pore structure characteristics of the material. As depicted in Fig. 3(e), MNSAC exhibited a Type I isotherm with a steep rise in adsorption capacity at low pressures followed by a plateau, indicating a micropore-dominated structure where micropores constitute 88.0% of the total pore volume (Table S4). However, it is well established that an excessively high micropore fraction increases ionic transport resistance, adversely affecting rate performance. In contrast, F-MNSAC displayed a Type IV isotherm accompanied by pronounced hysteresis loops, indicating successful introduction of mesopores. The pore size distribution curve confirmed the enhanced mesoporous structure within F-MNSAC (Fig. 3f, Fig. S8). The hierarchical micro-mesoporous structure of F-MNSAC can be attributed to two synergistic mechanisms. (i) During the activation stage, the pore-forming effect of KOH generates a large number of micropores, while some of these micropores expand into mesopores. (ii) During the passivation-stage grafting process, when C=O groups are selectively replaced by :$CF_2$ accompanied by CO release, the gas generation causes local etching or fusion of adjacent micropore walls, effectively converting some of the micropores into small mesopores. Mesopores serve as crucial pathways for electrolyte ion transport, and act as bridges between bulk electrolyte and micropore active sites [47,48]. Consequently, an appropriate increase in mesopore proportion can optimize the pore structure in conjunction with micropores, which can facilitate electrolyte ion diffusion from the electrode surface into the bulk phase, effectively boosting ion transfer efficiency and fully realizing the energy storage potential of micropores. Due to the higher total pore volume ($V_{total}$, 1.213 $cm^3\ g^{-1}$), F-MNSAC exhibits a higher specific surface area ($S_{BET}$) of 2179.8 $m^2\ g^{-1}$ than MNSAC (Table S4). The high $V_{total}$ provides direct evidence that the fluoridation process and high compaction density (0.64 g $cm^{-3}$) do not compromise the internal pore structure. Moreover, the increased $S_{BET}$ offers more abundant ion adsorption sites, suggesting that F-MNSAC may possess a higher charge storage capacity.

### 2.2. Electrochemical performance of F-MNSAC-based supercapacitors

To systematically evaluate the electrochemical performance of the samples, we constructed symmetrical button-type supercapacitors based on F-MNSAC and MNSAC, and conducted testing in a 1 M $Et_4NBF_4$/AN organic electrolyte system. Cyclic voltammetry

(CV) tests provided insight into the charge storage behavior. As shown in Fig. 4(a), the CV curves of F-MNSAC maintained a quasi-rectangular shape at various scan rates (20–1000 mV $s^{-1}$), without distinct redox peaks, which indicated that the introduction of the F atom did not induce a significant pseudocapacitive effect, so the energy storage mechanism remained dominated by double-layer physical adsorption/desorption. In contrast, at the high scan rate of 1000 mV $s^{-1}$, the CV curve of MNSAC exhibited a triangular shape (Fig. 4b), correlating with its lower mesopore content, which resulted in delayed ion transport kinetics during high-current impact. Electrochemical impedance spectroscopy (EIS) was employed to measure the impedance response of the supercapacitors as a function of frequency at a constant potential. The Nyquist plots of both devices exhibited typical double-layer capacitance characteristics, comprising a semicircle in the high-frequency region, a 45° slope in the mid-frequency region, and a near-vertical line in the low-frequency region. The diameter of the semicircle reflects charge transfer resistance ($R_{ct}$), representing the energy barrier for charge transfer at the electrode/electrolyte interface. Besides, the closer the slope of the low-frequency region line approaches 90°, the more the capacitive behavior approximates an ideal double layer [49]. As shown in Fig. 4(c), F-MNSAC-based supercapacitor exhibits a smaller semicircle diameter, corresponding to a lower $R_{ct}$ of 0.67 Ω compared to 1.31 Ω for MNSAC (Fig. S9). This quantitative result is consistent with the higher electrical conductivity of F-MNSAC. Its low-frequency region line approaches verticality, indicating superior double-layer response characteristics. The frequency response behavior of the devices was further analyzed using Bode plots (Fig. 4d). Compared to MNSAC, F-MNSAC exhibited lower impedance modulus and a phase angle closer to 90° in the low-frequency region, while its phase angle approaches 0° in the high-frequency region, which reflected its superior ion diffusion capability and more rapid capacitive response. From this perspective, F-MNSAC is indeed well-suited for high-rate charge/discharge scenarios. Furthermore, the characteristic relaxation time constant ($\tau_0$) was calculated based on the frequency corresponding to a phase angle of 45°. As shown in Fig. S10, F-MNSAC exhibited a $\tau_0$ of merely 0.50 s, significantly lower than MNSAC ($\tau_0$ = 0.79 s), confirming its faster electrode kinetics. Galvanostatic charge/discharge (GCD) testing serves as a pivotal method for evaluating supercapacitor capacitance. Ideal GCD curves exhibit a symmetrical, isosceles-triangular shape, with their area directly reflecting energy storage capacity. Notably, the GCD curves of F-MNSAC-based supercapacitor at various current densities (1–50 A $g^{-1}$) all displayed highly symmetrical, triangular profiles (Fig. S11), attributable to its outstanding electrochemical reversibility. Under the same organic electrolyte and device testing conditions, the specific capacitance of F-MNSAC reached 33.63 F $g^{-1}$ at 1 A $g^{-1}$ (Fig. 4e and Table S5), outperforming MNSAC (31.83 F $g^{-1}$) and commercialized YP-50F (~27 F $g^{-1}$) [47]. With increasing current density, the gap in specific capacitance between the two materials progressively widened. At the highest current density of 50 A $g^{-1}$, F-MNSAC maintained a capacitance retention rate of 86.6%, markedly superior to MNSAC (70.7%), demonstrating remarkable rate capability. The difference in capacitance can be seen intuitively in Fig. 4(f). This excellent rate performance is closely related to the intrinsic F-induced effect. Unlike heteroatoms such as N or S, which can participate in reversible redox reactions and contribute pseudo-capacitance through Faradaic charge transfer, the polar covalent C–F bonds formed by F within the carbon matrix cause a redistribution of local electron density without introducing Faradaic reactions, as evidenced by the absence of distinct redox peaks in the CV curves [50]. Therefore, the enhanced rate performance of F-MNSAC should be attributed to improvements in conductivity and increased ion affinity due to surface polarization effects, rather than pseudocapacitive contributions. The GCD curves typically reveal an instantaneous voltage drop during state transition, which can reflect the internal resistance of supercapacitors. As shown in Table S6, F-MNSAC exhibited a voltage drop of merely 6.78 mV at 1 A $g^{-1}$, substantially lower than MNSAC (10.41 mV). indicating a lower equivalent series resistance, which helped F-MNSAC maintain a smaller voltage drop even under high-rate conditions (0.25 V at 50 A $g^{-1}$). Evaluated in terms of energy and power density (based on the total mass of the symmetric supercapacitor device), the Ragone plot (Fig. S12) indicated that F-MNSAC achieved a high energy density of 33.9 Wh $kg^{-1}$ and a power density of 1.3 kW $kg^{-1}$. Even at a higher power density of 61.2 kW $kg^{-1}$, its energy density remained at a high value of 24.1 Wh $kg^{-1}$, surpassing MNSAC (16.7 Wh $kg^{-1}$, 57.7 kW $kg^{-1}$). Furthermore, as summarized in Table S7, F-MNSAC outperforms most recently reported carbon-based electrodes in terms of rate capability and energy-power synergy in organic electrolytes (Fig. S13), which could be attributed to the improved electroconductivity and pores in F-MNSAC, highlighting the effectiveness of the difluorocarbene grafting strategy [51–69]. To investigate the morphological changes of the electrodes after long-term cycling, SEM characterization was performed on the harvested electrodes. As shown in Fig. S14, both electrode surfaces exhibit particle fusion-like features, which could be attributed to a passivation layer formed by the decomposition of acetonitrile solvent, OCFGs, and adsorbed water molecules under a high voltage. Notably, F-MNSAC exhibits significantly fewer fused regions compared to MNSAC, suggesting that fluorination effectively mitigates interfacial side reactions. Different from MNSAC, the F-MNSAC electrode exhibited fewer fusion zones and improved interparticle connectivity. This advantage originated from partial replacement of OCFGs during the fluorocarbon substitution process, which reduced interfacial side reactions and enhanced the chemical stability at the electrode/electrolyte interface. In order to more clearly illustrate the state of the electrode/electrolyte interface after cycling, post-cycling XPS analysis was conducted (Fig. S15). Compared with MNSAC, the F-MNSAC electrode has a higher concentration of carbon frameworks (C–C/C=C), indicating a thinner electrode/electrolyte interface. Meanwhile, the F-MNSAC electrode exhibits higher C–O/C–N and lower C=O concentrations, suggesting that the fluorinated surface can guide the electrolyte towards more stable decomposition products during cycling. Cycling stability is a crucial metric for assessing the practical value of supercapacitors. As shown in Fig. 4(g), after 10,000 cycles at 5 A $g^{-1}$, the F-MNSAC-based supercapacitor exhibited a capacity decay rate of merely 11%, significantly lower than 25% observed for MNSAC, demonstrating exceptional stability. Furthermore, EIS analysis after cycling revealed that the impedance of F-MNSAC remained lower than that of MNSAC, which can be attributed to the high bond energy of the C–F bond enhancing the resistance of the electrode to degradation, ultimately retarding the ageing process and extending the cycling lifespan of devices. In summary, F-MNSAC-based supercapacitors exhibit excellent electrochemical performance, which can be intuitively demonstrated through a video showing that they directly power an light emitting diode (LED) light (Movie S1).

### 2.3. Mechanism for difluorocarbene grafted strategy to improve material properties

The synergistic optimization mechanism of material structure and performance achieved by our proposed difluorocarbene grafted strategy is that the introduction of highly electronegative F atoms into the carbon skeleton induced electron density redistribution, thereby reducing resistance to electron transport and ion diffusion. Besides, the structural defects introduced provided additional active sites for ion storage. The multi-faceted synergistic

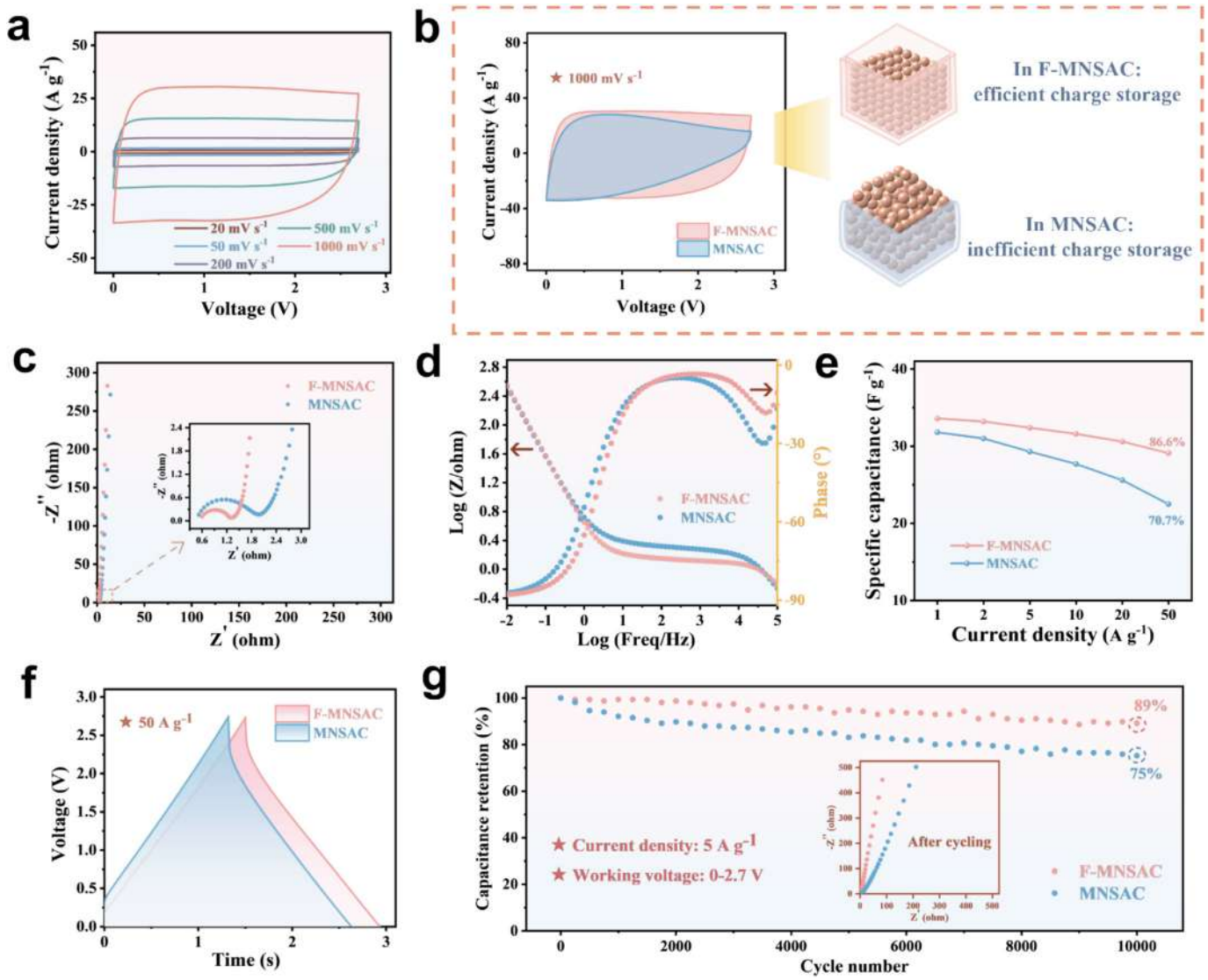



**Fig. 4.** Electrochemical performance of F-MNSAC-based and MNSAC-based supercapacitors. (a) CV curves at 20–1000 mV $s^{-1}$; (b) CV curves at 1000 mV $s^{-1}$; (c) Nyquist plots; (d) Bode plots; (e) specific capacitance at 1–50 A $g^{-1}$; (f) GCD curves at 50 A $g^{-1}$; (g) cycling performance at 5 A $g^{-1}$.

effect comprehensively enhanced the electrochemical performance of F-MNSAC. To validate the mechanism of enhanced interaction between fluorine-modified carbon material and electrolyte ions, we constructed structural models of MNSAC and F-MNSAC based on density functional theory (DFT), and performed calculations at the atomic scale. Electrostatic potential (ESP) analysis results, as shown in Fig. 5(a), revealed a uniform negative ESP distribution around the MNSAC model, while its interior exhibited a uniform positive ESP distribution. Following the incorporation of fluorocarbon molecules, the uniform charge distribution within and around F-MNSAC is disrupted. This disruption resulted in both maximum and minimum appearing around the F atom and its adjacent C atoms. This localized change in the electronic structure originates from the strong electronegativity of F. The incorporation of F effectively breaks the original symmetry of charge distribution, promoting the highest occupied molecular orbital (HOMO) orbital electron delocalization and spin density rearrangement. Further quantitative surface ESP analysis (Fig. 5b) reveals an overall negative shift and a distribution concentrated in the range of 0–10 kcal $mol^{-1}$ for F-MNSAC, confirming its optimized surface charge characteristics. Differential charge density plots at the top of Fig. 5(c) visually demonstrated the redistribution of electron density in F-MNSAC following F incorporation. We further calculated the adsorption binding energies of both carbon configurations with the organic electrolyte ion $(CH_3CH_2)_4N^+$ via first-principles calculations (bottom of Fig. 5c). Both F-MNSAC and MNSAC exhibited negative binding energies with $(CH_3CH_2)_4N^+$, indicating thermodynamically spontaneous adsorption of a physical nature. Notably, the absolute value of the F-MNSAC binding energy reaches 3.65 eV, significantly higher than 1.83 eV for MNSAC (Fig. 5d). This indicates that F introduction substantially enhanced the adsorption capacity of the electrode material for electrolyte ions, thereby improving charge storage efficiency. These theoretical results can be directly associated with XPS bonding states, thereby elucidating charge transfer dynamics. The covalent C–F bonds (Fig. 2h), due to the transition from $sp^2$ to $sp^3$ hybridization, induce local lattice distortion and generate atomic-scale strain near the grafted :$CF_2$ groups. This strain modulates the surrounding charge density distribution, forming local electron-rich and electron-deficient regions, thereby facilitating carrier migration. This strain-mediated charge redistribution has been established as an effective mechanism for enhancing the electronic conductivity of doped systems [70]. Theoretical calculations consistently indicated that the difluorocarbene grafting strategy multi-dimensionally enhanced charge

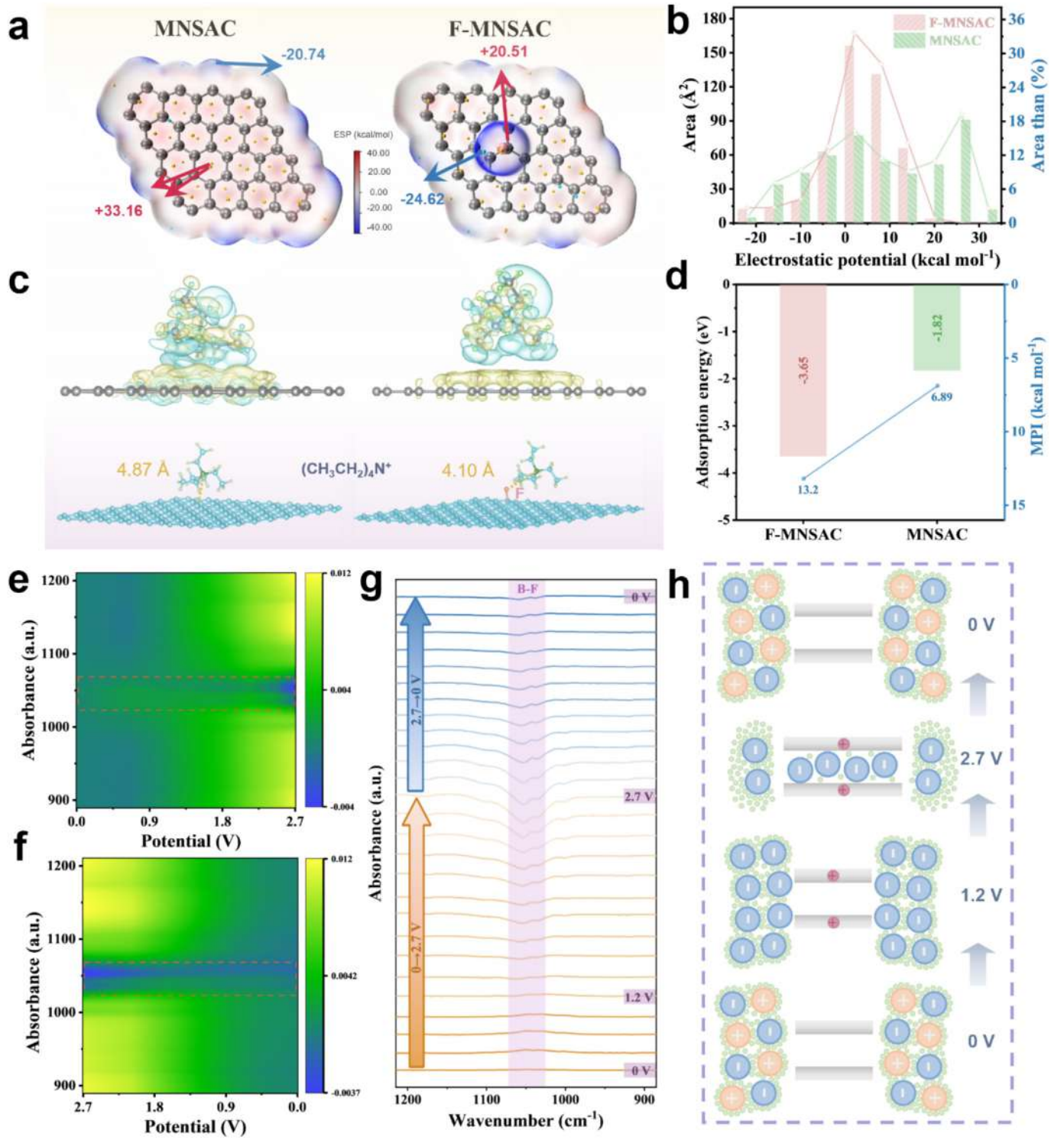



**Fig. 5.** (a) Electrostatic potential maps; (b) surface electrostatic potential distribution; (c) adsorption configurations of electrolyte ions (top) and charge density difference plots (bottom); (d) calculated adsorption energy values of F-MNSAC and MNSAC; in-situ electrochemical FT-IR spectra collected during (e) charging from 0 to 2.7 V and (f) discharging from 2.7 to 0 V; (g) voltage-dependent FT-IR spectra; (h) proposed ion transfer mechanism.

transport efficiency and interfacial ion adsorption kinetics of the material by modulating the electronic structure, optimizing the surface potential, and strengthening ion adsorption. This provided a profound theoretical basis for understanding the exceptional electrochemical performance of F-MNSAC.

Traditional electrochemical methods primarily provide macroscopic information about the reaction processes of activated carbon electrodes, falling short of revealing the microscopic mechanisms underlying interfacial ion dynamics and charge storage. To investigate the ion migration patterns within F-MNSAC-based supercapacitors during charge-discharge cycles, we employed in-situ FT-IR to provide unique insights. The intensity variation of the B–F characteristic peak (approximately 1050–1100 $cm^{-1}$) effectively characterizes changes in electrolyte concentration at the elec-

trode/electrolyte interface [71,72]. As depicted in Fig. 5(e–g), a distinct positive absorption peak emerged during charging from 0 to 1.2 V, with peak intensity gradually increasing with voltage. Upon further voltage elevation from 1.2 to 2.7 V, the absorption peak reverses, exhibiting rapid intensity enhancement with increasing voltage. The discharge process exhibits a fundamentally analogous inverse sequence. Based on these findings, we propose distinct ion migration mechanisms for different voltage regions shown in Fig. 5 (h) (using the charging process as an example). (i) Low-voltage region (0–1.2 V): under the action of an electric field, $BF_4^-$ anions in the electrolyte migrated towards the cathode while $(CH_3CH_2)_4N^+$ cations migrated towards the anode. These ions aggregated at the macropores or mesopores, gradually forming a double layer. Under weaker electric fields, ions remained in a solvated state enveloped by acetonitrile molecules. This resulted in higher electrolyte concentrations at the interface compared to the bulk phase, creating an electrolyte concentration gradient that increased with intensifying electric fields. (ii) Critical voltage process (~1.2 V): when the voltage rose to about 1.2 V, ions gained sufficient energy to overcome the interaction with solvent molecules. The value of this critical voltage is directly determined by the micropore entrance size and the surface properties modified by fluorination. The physical size of the micropores (<2 nm) restricts entry to ions that have partially desolvated and reduced in size. Meanwhile, the strongly polar surface introduced by C–F bonds optimizes the local electric field and chemical environment at the interface, collaboratively lowering the energy barrier required for ions to remove part of their solvent molecules. Therefore, under an electric field of approximately 1.2 V, ions gain sufficient energy to complete desolvation and embed into the micropores, resulting in the relative enrichment of solvent molecules at the electrode/electrolyte interface and a corresponding relative decrease in $BF_4^-$ concentration, which corresponds to the transition from positive to negative peaks in FT-IR spectra. It is noteworthy that the ~1.2 V identified by in-situ FT-IR is a characteristic voltage transition region, marking the prominent onset of the ion desolvation process. Since this process occurs continuously over a certain voltage range, the macroscopic GCD curve does not show a sharp inflection point, but remains smooth. (iii) High-voltage process (1.2–2.7 V): under intense electric fields, desolvation became the dominant mechanism. As voltage increased, desolvation deepened progressively, with more ions entering micropores to achieve higher charge storage densities. The ion concentration at the electrode/electrolyte interface, which possesses a complete solvation shell, decreases rapidly. This migration mechanism demonstrated that designing a multi-level pore structure with optimally proportioned "ion highways" (mesopores) and "ion parking lots" (micropores) can significantly enhance the ion kinetic response characteristics on the electrode surface. This provided a rational explanation for how F-MNSAC-based supercapacitors simultaneously achieved high specific capacitance and excellent rate performance. Naturally, the outstanding electrochemical performance exhibited by F-MNSAC stems not only from its advantageous pore size structure but also from its unique interfacial characteristics. As introduced earlier, the incorporation of the F element optimized the electronic conductivity of F-MNSAC while enhancing the adsorption force of electrolyte ions on the electrode surface through the formation of highly polar C–F covalent bonds. These synergistic effects markedly reduce the ion transport energy barrier, enabling the material to maintain efficient charge storage capacity even under high-rate charge-discharge conditions.

## 3. Conclusions

In summary, this work innovatively develops a difluorocarbene-grafted strategy for modifying MNSAC. We systematically elucidated the structure-property relationship between the physicochemical characteristics of the material and its electrochemical performance, establishing a theoretical model for F-enhanced electrolyte ion adsorption. The highly electronegative F functional groups are grafted onto the carbon skeleton. This induces a pronounced redistribution of electron density across the MNSAC framework due to a strong electron-withdrawing effect, which expands the charge carrier mobility domain and substantially enhances electrical conductivity. Concurrently, the incorporated F atoms exert a controlled etching effect on the carbon skeleton via CO release during the selective substitution of C=O groups, which promotes the partial conversion of micropores into mesopores and thereby rationally tailors the pore hierarchy for enhanced ion transport. This tailored porosity significantly accelerates electrolyte ion diffusion and optimizes the charge storage capability of the micropores. The optimized material, F-MNSAC, demonstrates a high electrical conductivity of 3.34 S $mm^{-1}$ and a substantial pore volume of 1.213 $m^3$ $g^{-1}$. Leveraging these exceptional properties, a supercapacitor based on F-MNSAC delivers outstanding electrochemical performance: a specific capacitance of 33.63 F $g^{-1}$ at 1 A $g^{-1}$, an exceptional rate capability with 86.6% capacitance retention at 50 A $g^{-1}$, and remarkable power and energy densities of 61.2 kW $kg^{-1}$ and 24.1 Wh $kg^{-1}$, respectively. These results surpass those of many reported ACs-based supercapacitors. The underlying kinetic mechanism, validated through theoretical calculations and in-situ FT-IR spectroscopy, confirms the role of F atoms in enhancing ion transport kinetics. This work successfully demonstrates the synergistic design of surface chemistry and pore architecture in biomass-derived ACs, providing a significant advancement in the development of high-performance, high-power supercapacitors.

## Experimental section

Experimental details can be found in the Supporting Information.

## CRediT authorship contribution statement

**Kai Gu:** Writing – original draft, Methodology, Investigation, Formal analysis, Data curation, Conceptualization. **Zhenyu Chen:** Writing – original draft, Investigation, Formal analysis, Data curation. **Yuxun Yuan:** Visualization, Software. **Ting Yang:** Investigation, Data curation. **Yihan Wang:** Project administration, Investigation. **Lei Zhou:** Investigation. **Lingchao Wu:** Investigation. **Guilin Feng:** Writing – review & editing, Supervision, Resources, Project administration, Funding acquisition, Conceptualization. **Weiqing Yang:** Writing – review & editing, Validation, Supervision, Resources, Funding acquisition.

## Declaration of competing interest

The authors declare that they have no known competing financial interests or personal relationships that could have appeared to influence the work reported in this paper.

## Acknowledgments

This work was supported by the National Natural Science Foundation of China (No. 52372228, No. 22309203); the Science and Technology Department project of Sichuan Province of China (No. 2024ZYD0013); the China Postdoctoral Science Foundation (2024M752669); the Sichuan Science and Technology Program (No. 2026NSFSC0896); the Fundamental Research Funds for the Central Universities (Grant Number: 2682025CX003).

## Appendix A. Supplementary material

Supplementary data to this article can be found online at https://doi.org/10.1016/j.jechem.2026.03.057.

## References


[1] M. Salanne, B. Rotenberg, K. Naoi, K. Kaneko, P.L. Taberna, C.P. Grey, B. Dunn, P. Simon, Nat. Energy 1 (2016) 16070.
[2] S. Seenivasan, A.T. Sivagurunathan, D. Kim, Energy Storage Mater. 70 (2024) 103482.
[3] T.M. Mo, Z.X. Wang, L. Zeng, M. Chen, A.A. Kornyshev, M.C. Zhang, Y.Q. Zhao, G. Feng, Adv. Mater. 35 (2023) 2301118.
[4] H.R. Liu, X.T. Chen, Y.M. Zhou, Y.H. Lv, W. Zhang, D.D. Jia, H.L. Wang, Coord. Chem. Rev. 551 (2026) 217485.
[5] G. Dhakal, D.R. Kumar, S. Sahoo, J.J. Shim, Carbon 208 (2023) 277–289.
[6] B. Réty, H.Y. Yiin, C.M. Ghimbeu, Energy Storage Mater. 74 (2025) 103963.
[7] Y.H. Lv, H.R. Liu, B. Li, W. Zhang, J. Qiao, L.B. Ma, F. Wei, Chem. Commun. 61 (2025) 9596–9609.
[8] O. Soto-Díaz, D.R. Lobato-Peralta, A. Ayala-Cortés, H.I. Villáfan-Vidales, S.A. Gamboa-Sanchez, V.H. Collins-Martínez, M. Román-Aguirre, G. González-García, A.K. Cuentas-Gallegos, V.H. Ramos-Sánchez, Chem. Eng. J. 507 (2025) 160743.
[9] R. Yuksel, N. Karakehya, Carbon 221 (2024) 118934.
[10] D. Dong, Y. Xiao, Chem. Eng. J. 470 (2023) 144441.
[11] P. Dubey, V. Shrivastav, P.H. Maheshwari, S. Sundriyal, Carbon 170 (2020) 1–29.
[12] W. Sun, S.M. Lipka, C. Swartz, D. Williams, F.Q. Yang, Carbon 103 (2016) 181–192.
[13] S.J. Wu, H.J. Li, D.N. Futaba, G.H. Chen, C. Chen, K.C. Zhou, Q.F. Zhang, M. Li, Z.L. Ye, M. Xu, Adv. Mater. 34 (2022) 2201046.
[14] W.L. Zhang, J. Yin, W.B. Jian, Y. Wu, L.H. Chen, M.L. Sun, U. Schwingenschlögl, X. Q. Qiu, H.N. Alshareef, Nano Energy 103 (2022) 107827.
[15] Q. Liu, D.L. Wu, T. Wang, C.G. Wang, D.Z. Jia, Adv. Funct. Mater. 34 (2024) 2400556.
[16] J. Huang, Y.P. Xie, Y. You, J.L. Yuan, Q.Q. Xu, H.B. Xie, Y.W. Chen, Adv. Funct. Mater. 33 (2023) 2213095.
[17] Y.X. Xu, Z.Y. Lin, X. Zhong, X.Q. Huang, N.O. Weiss, Y. Huang, X.F. Duan, Nat. Commun. 5 (2014) 4554.
[18] Y.Y. Long, X.Y. An, H. Zhang, J. Yang, L.Q. Liu, Z.J. Tian, G.H. Yang, Z.B. Cheng, H. B. Cao, H.B. Liu, Y.H. Ni, Chem. Eng. J. 451 (2023) 138877.
[19] X.H. Zhang, R.Y. Han, Y.Z. Liu, H.X. Li, W.J. Shi, X.Y. Yan, X.X. Zhao, Y.F. Li, B.S. Liu, Chem. Eng. J. 460 (2023) 141607.
[20] P.P. Yu, Z.M. Zhang, L.X. Zheng, F. Teng, L.F. Hu, X.S. Fang, Adv. Energy Mater. 6 (2016) 1601111.
[21] W.L. Zhang, C. Xu, C.Q. Ma, G.X. Li, Y.Z. Wang, K.Y. Zhang, F. Li, C. Liu, H.M. Cheng, Y.W. Du, N.J. Tang, W.C. Ren, Adv. Mater. 29 (2017) 1701677.
[22] B. Li, F. Dai, Q.F. Xiao, L. Yang, J.M. Shen, C.M. Zhang, M. Cai, Energy Env. Sci. 9 (2016) 102–106.
[23] X.Y. Qian, L. Miao, J.X. Jiang, G.C. Ping, W. Xiong, Y.K. Lv, Y.F. Liu, L.H. Gan, D.Z. Zhua, M.X. Liu, Chem. Eng. J. 388 (2020) 124208.
[24] Z.X. Xu, Z. Sun, J.A. Shan, S. Jin, J.Y. Cui, Z.P. Deng, M.H. Seo, X.L. Wang, Adv. Funct. Mater. 34 (2024) 2313443.
[25] V.S. Kale, M. Hwang, H. Chang, J. Kang, S.I. Chae, Y. Jeon, J. Yang, J. Kim, Y.J. Ko, Y.Z. Piao, T. Hyeon, Adv. Funct. Mater. 28 (2018) 1803786.
[26] W. Lei, J.P. Guo, Z.X. Wu, C.J. Xuan, W.P. Xiao, D.L. Wang, Sci. Bull. 62 (2017) 1011–1017.
[27] D.H. Li, G.J. Chang, L. Zong, P. Xue, Y. Wang, Y.Z. Xia, C. Lai, D.J. Yang, Energy Storage Mater. 17 (2019) 22–30.
[28] Y. Sim, S. Surendran, H. Cha, H. Choi, M. Je, S. Yoo, D.C. Seok, Y.H. Jung, C. Jeon, D.J. Kim, M.K. Han, H. Choi, U. Sim, J. Moon, Chem. Eng. J. 428 (2022) 132086.
[29] T. Wang, X.B. Zang, X.M.Z. Wang, X.X. Gu, Q.G. Shao, N. Cao, Energy Storage Mater. 30 (2020) 367–384.
[30] L.Q. Huang, Z.Y. Luo, M.W. Luo, Q. Zhang, H. Zhu, K.Y. Shi, S.P. Zhu, J. Energy Storage 38 (2021) 102509.
[31] B.B. Liu, J.G. Hou, K. Wang, C.X. Xu, Q.H. Zhang, L. Gu, W.J. Zhou, Q. Li, J. Wang, H. Liu, Adv. Sci. 11 (2024) 2402033.
[32] S. Ghosh, S. Barg, S.M. Jeong, K. Ostrikov, Adv. Energy Mater. 10 (2020) 2001239.
[33] W.C. Lai, X. Wang, J.M. Fu, T. Chen, K. Fan, X.Y. Liu, Carbon 137 (2018) 451–457.
[34] S.Z. Huang, Y. Li, Y.Y. Feng, H.R. An, P. Long, C.Q. Qin, W. Feng, J. Mater. Chem. A 3 (2015) 23095–23105.
[35] V. Satulu, M.D. Ionita, S. Vizireanu, B. Mitu, G. Dinescu, Molecules 21 (2016) 1711.
[36] W. Zhang, K. Guérin, M. Dubois, Z. El Fawal, D.A. Ivanov, L. Vidal, A. Hamwi, Carbon 46 (2008) 1010–1016.
[37] H. Yamamoto, K. Tada, J. Hwang, D. Hirai, Z. Hiroi, K. Matsumoto, R. Hagiwara, Inorg. Chem. 62 (2023) 2116–2127.
[38] J. Demaison, L. Margulès, J.M.L. Martin, J.E. Boggs, Phys. Chem. Chem. Phys. 4 (2002) 3282–3288.
[39] F. Rodriguez-Reinoso, M. Molina-Sabio, Adv. Colloid Interface Sci. 76 (1998) 271–294.
[40] A.P. Charmet, P. Stoppa, S. Giorgianni, S. Ghersetti, J. Mol. Struct. 599 (2001) 31–38.
[41] H.W. Yu, W.R. Han, L. Liu, D.D. Gu, W. Mu, N. Chen, Mater. Rep. 24 (2014) 95–98.
[42] K.L. Zhang, J. Huang, G. Yu, Q.W. Zhang, S.B. Deng, B. Wang, Environ. Sci. Technol. 47 (2013) 6471–6477.
[43] G.L. Feng, X.H. Liu, C.L. Xu, R.M. Sun, J.Y. Wang, X. Yang, Y.B. Wang, Z.H. Wang, Y.X. Chen, W.Q. Yang, Energy Storage Mater. 82 (2025) 104559.
[44] F. Yuan, H.L. Sun, D. Zhang, Z.J. Li, J. Wang, H. Wang, Q.J. Wang, Y.S. Wu, B. Wang, J. Colloid Interface Sci. 611 (2022) 513–522.
[45] R.S. Xu, M.J. Hou, Y. Wang, L. Li, Z.L. Pan, C.W. Song, T.H. Wang, Carbon 201 (2023) 24–36.
[46] G.L. Feng, X. Yang, X.H. Liu, Y.B. Wang, Y.T. Xie, P.P. Dong, X.X. Jiao, C.L. Xu, J.M. Zhao, Y.S. Hu, W.Q. Yang, Nano Energy 136 (2025) 110728.
[47] Q. Wang, Y.X. Qu, Y.X. Yuan, Z.Y. Chen, G.L. Feng, P.P. Dong, X.X. Jiao, Y.L. Zou, W.Q. Yang, Adv. Mater. 37 (2025) 2418997.
[48] P. Simon, Y. Gogotsi, Nat. Mater. 7 (2008) 845–854.
[49] C.F. Shao, S.J. Qiu, G.M. Wu, B.Y. Cui, H.L. Chu, Y.J. Zou, C.L. Xiang, F. Xu, L.X. Sun, Carbon Energy 3 (2021) 361–374.
[50] W. Li, W.H. Zhang, Y. Xu, G.H. Wang, W.J. Sui, T. Xu, Z.H. Yuan, C.L. Si, Chem. Eng. J. 497 (2024) 154829.
[51] R.R. Zhao, J. Hao, X. Yang, Y. Zhao, J.N. Chen, J.L. Guo, C.X. Chi, Q.J. Guo, J. Power Sources 623 (2024) 235436.
[52] B.K. Sun, X.Y. Zhang, X. Fan, R.Y. Wang, H.C. Bai, X.Y. Wei, Energy 249 (2022) 123659.
[53] Z.Y. Zou, W. Liu, P.J. Li, X.L. Li, Mater. Rep. 39 (2025) 23080193.
[54] Y. Wu, J.P. Cao, Z. Zhou, Q.Q. Zhuang, Y.L. Wei, X.Y. Zhao, J. Fuel Chem. Technol. 49 (2021) 537–545.
[55] Q.Q. Zhuang, J.P. Cao, Y. Wu, Y.L. Wei, Z.H. Yang, X.Y. Zhao, J. Fuel Chem. Technol. 50 (2022) 408–417.
[56] H.C. Liu, W.H. Shi, H. Song, Y.Z. Chang, L.P. Feng, W.J. Hou, Y.P. Li, Y. Zhao, S. Zhu, G.Y. Han, ACS Appl. Energy Mater. 6 (2023) 222–232.
[57] S. Pappu, S. Anandan, T.N. Rao, S.K. Martha, S. Bulusu, J. Energy Storage 50 (2022) 104598.
[58] P.P. Chang, J. Zheng, Y.B. Cen, F. Yang, X.G. Li, Q.R. Xie, J.S. Dong, J. Power Sources 533 (2022) 231413.
[59] M. Bora, D. Bhattacharjya, S. Hazarika, X. Fan, B.K. Saikia, Energ. Fuels 36 (2022) 14476–14489.
[60] J. Zhang, H.C. Yang, Z.S. Huang, H.H. Zhang, X.C. Lu, J.H. Yan, K.F. Cen, Z. Bo, Waste Dispos. Sustain. Energy 5 (2023) 417–426.
[61] R. Ma, G.F. Fu, L.L. Ai, M.J. Xu, N.N. Guo, L.X. Wang, Int. J. Biol. Macromol. 307 (2025) 142320.
[62] S.A. Ageeb, A. Alrubayyi, L.M. Mokhtar, A.Q. Alshammari, I.A. Salim, H.A. Hamouda, ChemistrySelect 10 (2025) e04548.
[63] Y. Yao, T. Xie, P.Y. Li, W.E. Du, J.H. Jiang, H. Ding, T. Zhao, G.C. Xu, L. Zhang, Diam. Relat. Mater. 138 (2023) 110169.
[64] K.M. Dong, J.J. Wang, F.Q. Guo, S. Liu, B. Tang, L.W. Kong, N.J. Zhao, Y.T. Hou, Diam. Relat. Mater. 140 (2023) 110531.
[65] S.B. Liu, Q.S. Zhang, J.N. Liu, J.R. Li, W.J. Liu, Y. Wang, S.J. Yuan, Int. J. Mol. Sci. 25 (2024) 7583.
[66] J.F. Tu, Z.J. Qiao, Y.Z. Wang, G.F. Li, X. Zhang, G.P. Li, D.B. Ruan, Int. J. Electrochem. Sci. 18 (2023) 16–24.
[67] H.R. Zhang, M.X. Zhu, J.P. Zhou, J. Energy Storage 66 (2023) 107406.
[68] M.W. Hameed, A.M. Khan, Z. Ali, S. Majeed, Y. Abbas, W. Liu, G.X. Chen, T. Zhang, Z.P. Wu, J. Electroanal. Chem. 981 (2025) 119006.
[69] M. Mushtaq, M. Koroma, S. Jiang, S. Mathi, M.L. Tu, Z. Khanam, Y.W. Hu, J.Q. Deng, M.S. Balogun, J. Mater. Chem. A 13 (2025) 5933–5944.
[70] Y.F. Pang, L.Q. Wu, J. Liu, D.S. Tang, F. Xu, M.S. Cen, Z.H. Wang, Y.L. Xie, H. Yang, M.S. Balogun, Y.W. Hu, Adv. Funct. Mater. 35 (2025) 2506747.
[71] T. Yamada, M. Mizuno, ACS Omega 6 (2021) 1709–1717.
[72] T. Yamada, M. Mizuno, ACS Omega 7 (2022) 29804–29812.




**Kai Gu** received his B.S. from Southwest Jiaotong University in 2024. He is currently pursuing a doctoral degree in materials science and engineering at Southwest Jiaotong University. His research focuses on biomass carbon materials and electrochemical energy storage devices, such as supercapacitors and lithium/sodium-ion batteries.



**Guilin Feng** received his Ph.D. degree from Hokkaido University in 2023. Currently, he is a postdoctoral researcher in the Research Institute of Frontier Science at Southwest Jiaotong University. His research focuses on the development and exploration of biomass-derived hard carbon, the application of in-situ Raman characterization techniques in sodium-ion batteries.



**Weiqing Yang** received his M.S. in Physics in 2007, and Ph.D. in Materials Science and Engineering from Sichuan University in 2011. He was a post-doctorate research fellow at University of Electronic Science and Technology of China from 2011 to 2013. Subsequently, he was a post-doctorate research fellow at Georgia Institute of Technology from 2013 to 2014, under the supervision of Prof. Zhong Lin Wang. He is currently the Dean of the Research Institute of Frontier Science and a professor at the School of Materials Science and Engineering at Southwest Jiaotong University, with long-term research in the macroscopic preparation of special functional materials and cross-domain integration of intelligent equipment.